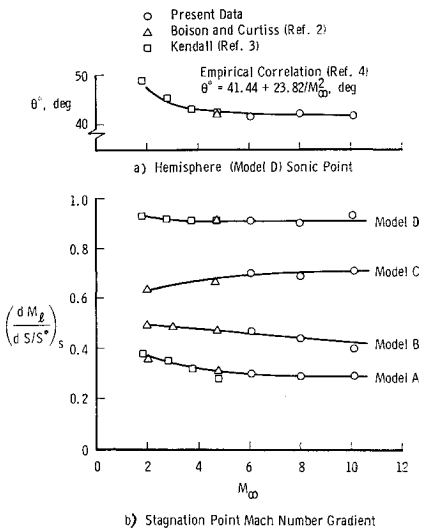

Fig. 3 Variation of spherical segment characteristics with freestream Mach number.

Mach number, and the experimental values presented in Fig. 3a were used.

The variation in local Mach number along the surface of the body was computed from the pressure distribution by assuming that the flow is an isentropic expansion of a perfect gas ($\gamma = 1.4$) with stagnation conditions equal to those behind the normal shock. The nondimensional stagnation-point Mach number gradient, $[dM_l/d\ (S/S^*)]_s$ was determined from these calculations and is presented in Fig. 3b as a function of freestream Mach number for each model. Comparison of the present results with the previously referenced lower Mach number data is made in Fig. 3b. A small interpolation of the data from Ref. 2 was required for comparison with model B. Agreement with the lower Mach number data is excellent, and Mach number independence above Mach 6 is demonstrated with the possible exception of model B. Conversion of the gradient $[dM_l/d\ (S/S^*)]_s$ to the dimensional velocity gradient $(dU/dS)_s$ is accomplished by the relation

$$[dU/dS]_s = [dM_l/d(S/S^*)]_s\ [a_s/S^*] \qquad (1)$$

An analytical expression for the stagnation-point Mach number gradient as developed from the modified Newtonian theory is

$$[dM_l/d(S/S^*)]_s = \theta^*[(2/\gamma)\ (1 - p_\infty/p_s)]^{1/2} \qquad (2)$$

Equation (2) suggests the use of θ^* as a bluntness correlation parameter for the stagnation-point Mach number gradient. The present data (M_∞ = 6–10) are correlated with bluntness (θ^*) in Fig. 4. The deviation of the data from the Newtonian prediction [Eq. (2)] is apparent as bluntness increases. The correlation does, however, provide a convenient and reasonably accurate means of predicting the stagnation-point velocity gradient for spherical segment bodies at hypersonic Mach numbers.

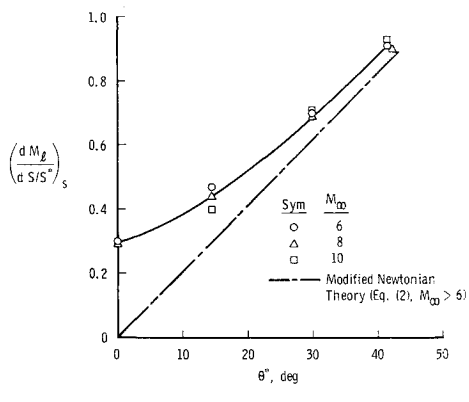

Fig. 4 Stagnation point Mach number gradient correlation with bluntness.

References

[1] Fay, J. A. and Riddell, F. R., "Theory of Stagnation Point Heat Transfer in Dissociated Air," *Journal of the Aerospace Sciences*, Vol. 25, No. 2, Feb. 1958, pp. 73–85.

[2] Boison, J. C. and Curtiss, H. A., "An Experimental Investigation of Blunt Body Stagnation Point Velocity Gradient," *ARS Journal*, Vol. 29, Feb. 1959, pp. 130–135.

[3] Kendall, J. M., Jr., "Experiments on Supersonic Blunt Body Flows," Progress Rept. 20–372, Feb. 1959, Jet Propulsion Lab., California Institute of Technology, Pasadena, Calif.

[4] Trimmer, L. L., "Study of the Blunt-Body Stagnation Point Velocity Gradient in Hypersonic Flow," TR-68-99 (AD669378), May 1968, Arnold Engineering Development Center.

Wind-Tunnel Diagnostics by Holographic Interferometry

J. K. Beamish,* D. M. Gibson,† and R. H. Sumner‡
General Dynamics, Fort Worth, Texas

and

S. M. Zivi§ and G. H. Humberstone‡
TRW Systems Group, Redondo Beach, Calif.

HOLOGRAPHIC interferograms have been made of flowfields about bullets in flight,[1] cones in wind tunnels,[2,3] and nozzle exhausts.[4,5]

Although the investigators in the aforementioned studies and others had established that holographic interferograms can be made, we conducted a number of experiments to determine whether the technique could be used routinely with a wind tunnel that was not designed specifically for the purpose of making holograms, and whether the advantages that holography is purported to offer are obtainable under normal operating conditions. The expected advantages that interested us most were 1) the ability to obtain large field interferograms without the prohibitive costs of large, high-quality optical components and tedious alignment of optical systems, 2) the three-dimensionality of holographic images, and, most important, 3) the ability to obtain interferograms of flowfields in such regions as corners and ducts where optical methods can be applied only by passing a light beam through a part of the model.

The last prospect is particularly significant because such information is becoming increasingly necessary in the design of modern, high-performance aircraft. It cannot be obtained by conventional shadowgraphic, schlieren, or interferometric methods because they would reveal all the distortion suffered by a light beam as it passed through both the flowfield and the transparent model, if there were one. In conventional techniques, the deformation of the wavefront caused by variations in the density of the air could not be

Received June 2, 1969.

* Senior Aerodynamics Engineer.
† Staff Scientist. Member AIAA.
‡ Senior Test Engineer.
§ Manager, Applied Optics Department.

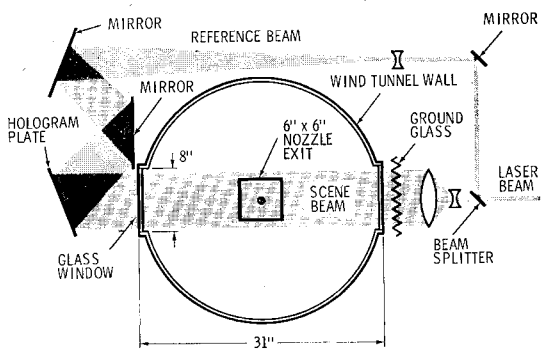

Fig. 1 Optical arrangement of holocamera around wind tunnel.

distinguished from the much greater deformation caused by any transparent components of the model.

We used a TRW Systems pulsed-ruby-laser holocamera, Model PRC-213, and conducted the experiments in the General Dynamics 6 × 6 in. supersonic freejet wind tunnel at Fort Worth. Test conditions were held nominally constant at Mach 4.0 and a Reynolds number of 4.6×10^6/ft.

Although discussions of holographic interferometry may be found in the literature, the procedure we used is outlined for the convenience of the reader.

Figure 1 is a schematic diagram of the wind tunnel and holocamera. Many optical components are omitted for simplicity. The reference and scene beams combine to form an interference pattern that is recorded in the emulsion of the photosensitive plate. The developed plate (hologram) is illuminated by a replica of the reference beam. A portion of this reconstruction beam is diffracted into a replica of the scene beam, i.e., it creates a virtual image of the entire scene from the scene illuminator (ground glass) to the photosensitive plate (hologram). It is this capability to capture a wavefront at one instant and release it later that makes holographic interferometry possible. An interferogram is made by exposing the plate twice. During the first exposure there is no flow in the tunnel but the pressure is approximately equal to the static pressure that will exist after the flow is established. The second exposure is made after flow is established. Illumination of the doubly exposed hologram with a replica of the reference beam produces images of the two exposures simultaneously. Wherever the density of the air changes during the time interval between the two exposures, the two reconstructed wavefronts will assume different shapes and, consequently, produce an interference pattern from which the density variations can be determined.

The first exposure is equivalent to the comparison beam in a Mach-Zehnder interferometer, and the second exposure is equivalent to the test beam. Because both beams follow the same path in the case of the doubly exposed hologram, distortion of the wavefronts by optically poor windows and transparent model components does not contribute to the fringe pattern; consequently, information about the flowfield is not degraded. We briefly describe the results of two of our experiments here.

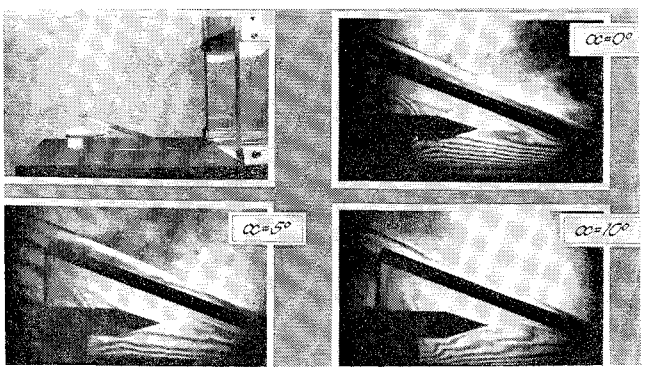

Fig. 2 Holographic interferograms through transparent model components. The delta wing is made of plexiglass and mounted on a turntable in a flat plate extension of the lower nozzle block. The three interferograms were made with the wing at angles of attack of 0°, 5°, and 10° as noted.

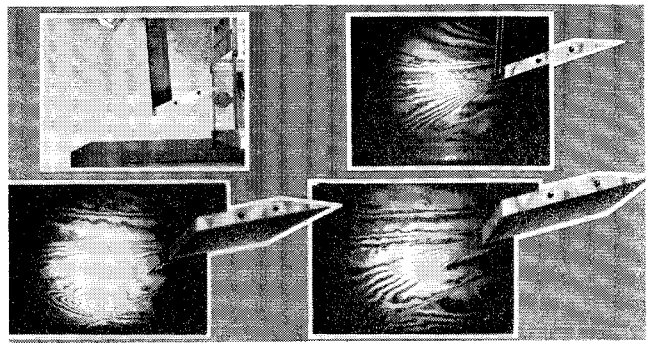

Fig. 3 Holographic interferograms of shock boundary-layer interaction. The three interferograms were made by photographing the reconstructed image from a single hologram. The interferograms represent three viewing perspectives of the shock generated by the wedge interacting with the thick boundary layer on a flat plate extension of the nozzle block.

Figure 2 shows a corner-flow experiment model and photographs of the reconstructed images of holographic interferograms of the flowfields for angles of attack of 0°, 5°, and 10°. The model consists of a flat-plate extension of the lower nozzle block, a Plexiglas delta-wing panel, and a cone-cylinder shock generator placed just above the flat-plate boundary layer and on the high-pressure side of the wing. The flat-plate boundary layer is visible as a series of nearly parallel fringes near the root of the delta wing. The effect of the cone-cylinder shock generator on the boundary-layer flow is clearly visible. The horseshoe-shaped fringes downstream of the cone-cylinder shoulder show the interaction of the conical shock with the boundary-layer flow on the surface of the wing. It should be noted that the image of the cone-cylinder seen through the transparent wing in the interferograms is comparable in quality to that of the photograph of the model.

Figure 3 graphically demonstrates the three-dimensionality of the holographic technique. The experiment consists of a wedge shock interaction with a thick boundary layer on a flat plate.

The interferograms shown here were made through 8-in.-diam schlieren-quality windows. Several holograms were made through 8 × 17-in. plate-glass windows with no discernible loss in the quality of the reconstructed image.

We have shown that useful holographic interferograms can be routinely obtained in the wind tunnel by use of transmission holography without the need for the high-optical-quality tunnel windows and the model components necessary with conventional interferometry. Further, these interferograms exhibit the three-dimensionality of holographic images and demonstrate the applicability of holographic interferometry to aerodynamic investigations of regions previously inaccessible to optical diagnostics.

References

[1] Heflinger, L. O., Wuerker, R. F., and Brooks, R. E., "Holographic Interferometry," *Journal of Applied Physics*, Vol. 37, Feb. 1966, pp. 642–649.

[2] Philbert, M. and Surget, J., "Application de L'interferometrie Holographique en Soufflerie," *La Recherche Aerospatiale*, Vol. 122, Jan.–Feb. 1968, pp. 55–60.

[3] Holds, J. H., "Aeronautical Applications of Holographic Interferometry," M.S. thesis, June 1967, U.S. Naval Postgraduate School, Monterey, Calif.

[4] Smigielski, P. and Royer, H., "Applications de L'holographie

a L'aerodynamique," *L'Onde Electrique*, Vol. 48, March 1968, pp. 223–225.

[5] Siebert, L. D. and Geister, D. E., "Pulsed Holographic Interferometry vs Schlieren Photography," *AIAA Journal*, Vol. 6, No. 11, Nov. 1968, pp. 2194–2195.

Generalized Stiffness Matrix of a Curved-Beam Element

HWA-PING LEE*
NASA Goddard Space Flight Center, Greenbelt, Md.

A CURVED-BEAM is a basic structural element; it represents many engineering structures either to be used alone or contained in a system with structural members of other elementary forms. When such a curved-beam element is employed in a space frame, the loads exerted at the nodes, i.e., the end points, are three-dimensional in the most general case. The stiffness matrix, which relates the forces to the displacements, is of the order of 12 × 12, because six general nodal forces exist at each node. The nodal forces comprise three rectilinear force components F_x, F_y, and F_z, one torsional moment M_x, and two bending moments M_y and M_z, among which F_x, F_y, and M_z are of the in-plane force components that lie in the plane containing the curved-beam element, and the remainders F_z, M_x, and M_y are of the normal-to-plane force components that produce, at any cross section of the curved-beam, the twisting and bending moments. It is a known fact that a stiffness matrix of a structure may be composed by constituent submatrices. The stiffness matrix of the in-plane force components is readily available,[1,2] but that of the normal-to-plane force components is not seen to exist in an explicit closed form. To find the generalized stiffness matrix of a curved-beam element is, therefore, reduced to seeking that submatrix of the force components of the second group. It is the purpose of this Note to present the generalized stiffness matrix with emphasis on the derivation of the stiffness matrix of the noncoupled normal-to-plane loads. The result may serve as a supplement to the subject matter treated in Ref. 2. Such a generalized stiffness matrix is of practical engineering importance, because it is a requisite to have a precise stiffness matrix when dynamic responses or internal forces of a structural system are sought. Furthermore, the closed form expressions can expedite hand calculation, especially for those who are unable to gain easy access to a digital computer to perform a matrix inversion.

A curved-beam element of uniform cross section is considered. Notations as well as directions of positive nodal forces and displacements are taken as shown in Fig. 1. Force vectors are represented by arrows, and moment vectors are represented according to the right-handed screw rule by a double arrowhead. The flexural stiffness calculated for a traverse cross section is represented by EI_y, and the torsional stiffness by GJ.

The derivation will proceed to obtain the flexibility matrix for the curved-beam element subjected to the set of normal-to-plane nodal forces at the left end with the right end being clamped. The corresponding displacements will be determined by introducing the strain energy U_n expressed in terms of the nodal forces, and then applying Castigliano's second theorem. When cross-sectional dimensions are taken as small compared with R, the total strain energy takes the form[3]

$$U_n = \frac{R}{2}\left(\int_0^\beta \frac{M^2}{EI_y}\,d\alpha + \int_0^\beta \frac{T^2}{GJ}\,d\alpha\right)$$

Received June 6, 1969.

* Aerospace Technologist, Space Simulation Research Section. Member AIAA.

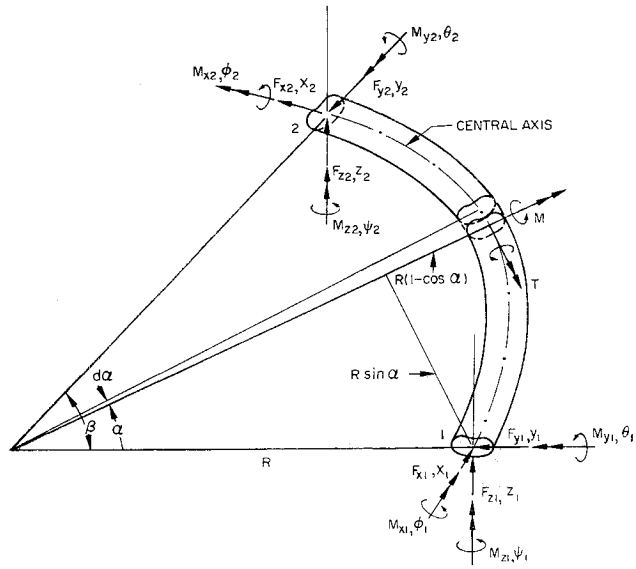

Fig. 1 Nodal forces and displacements relevant to a curved-beam element.

where the bending moment M and twisting moment T may be expressed as

$$M = -F_{z1}R\sin\alpha + M_{x1}\sin\alpha - M_{z1}\cos\alpha \qquad (1)$$

and

$$T = -F_{z1}R(1-\cos\alpha) - M_{x1}\cos\alpha - M_{z1}\sin\alpha \qquad (2)$$

Applying Castigliano's theorem gives the displacements at node 1 as

$$Z_1 = \frac{\partial U_n}{\partial F_{z1}} = \frac{R}{EI_y}\int_0^\beta M\frac{\partial M}{\partial F_{z1}}\,d\alpha + \frac{R}{GJ}\int_0^\beta T\frac{\partial T}{\partial F_{z1}}\,d\alpha$$

$$\phi_1 = \frac{\partial U_n}{\partial M_{x1}} = \frac{R}{EI_y}\int_0^\beta M\frac{\partial M}{\partial M_{x1}}\,d\alpha + \frac{R}{GJ}\int_0^\beta T\frac{\partial T}{\partial M_{x1}}\,d\alpha$$

$$\theta_1 = \frac{\partial U_n}{\partial M_{y1}} = \frac{R}{EI_y}\int_0^\beta M\frac{\partial M}{\partial M_{y1}}\,d\alpha + \frac{R}{GJ}\int_0^\beta T\frac{\partial T}{\partial M_{y1}}\,d\alpha$$

Carrying out the calculations with the aid of Eqs. (1) and (2) and then collecting terms into a single matrix equation give

$$\begin{Bmatrix} Z_1 \\ \phi_1 \\ \theta_1 \end{Bmatrix} = \frac{R^3}{EI_y}\begin{bmatrix} (\rho f + a) & (\rho d - a)\frac{1}{R} & (\rho e + b)\frac{1}{R} \\ (\rho d - a)\frac{1}{R} & (\rho c + a)\frac{1}{R^2} & (\rho - 1)\frac{b}{R^2} \\ (\rho e + b)\frac{1}{R} & (\rho - 1)\frac{b}{R^2} & (\rho a + c)\frac{1}{R^2} \end{bmatrix}$$

$$\begin{Bmatrix} F_{z1} \\ M_{x1} \\ M_{y1} \end{Bmatrix} = \frac{R^3}{EI_y}[\eta]\begin{Bmatrix} F_{z1} \\ M_{x1} \\ M_{y1} \end{Bmatrix}$$

where a ratio $\rho = EI_y/GJ$ has been incorporated, and the constants are defined as

$$a = \tfrac{1}{2}(\beta - \sin\beta\cos\beta) \qquad d = \sin\beta - c$$

$$b = \tfrac{1}{2}\sin^2\beta \qquad e = 1 - \cos\beta - b$$

$$c = \tfrac{1}{2}(\beta + \sin\beta\cos\beta) \qquad f = \beta - 2\sin\beta + c$$

Inverting the flexibility matrix $[\eta]$, which satisfies the reciprocal theorem, enables the nodal forces to be expressed in